

# Hydroelastic Analysis of 3D Printed Marine Propeller Working at Low Reynolds Number

Suraj Pawar<sup>1</sup>, Stefano Brizzolara<sup>2</sup>

<sup>1</sup>Department of Mechanical Engineering, Virginia Polytechnic Institute and State University

<sup>2</sup>Kevin T. Crofton Department of Aerospace and Ocean Engineering, Virginia Polytechnic Institute and State University

## ABSTRACT

A method to predict the hydro-elastic performance of 3D printed marine propeller operating at low Reynolds number is presented. The propeller of an Autonomous Underwater Vehicle (AUV) typically operates at lower Reynolds number due to their small size. At this low Reynolds number, the flow is in the laminar-turbulent transition region. The hydrodynamics of these propellers is different from the propeller which operates in fully turbulent flow. Also, the propeller of AUV is typically manufactured using 3D printing of plastic material. The 3D printed materials are not strong enough like metals or composite materials. We investigate the global and local hydrodynamic characteristic of model scale propeller using CFD RANSE solver with  $\gamma$ - $Re_0$  transition model. The twist of the propeller is calculated using a simple analytical expression based on the principle of torsional deflection. The performance of untwisted and twisted propeller are compared in terms of local flow characteristics like streamline pattern and global characteristics like hydrodynamic forces.

## Keywords

3D Printed Propeller, RANSE, Transition Model, Elastic Deformation

## 1 INTRODUCTION

There has been an increasing interest in using additive manufacturing technologies in the marine industry due to its advantage of shorter manufacturing time and lower cost. One such application is propeller manufactured using 3D printing plastic materials which are widely used in AUVs. The propeller of these AUVs usually operates at low Reynolds number (Portner 2014, Stanway et al 2006). Hence it is very important to study low Reynolds number hydrodynamic characteristics of the 3D printed propeller. However, very few researchers have worked on investigating low Reynolds number hydrodynamics of 3D printed propeller. Also, the work on the elastic behavior of 3D printed marine propeller is very limited.

Various experimental and computational studies have considered the hydro-elastic behavior of composite marine propeller. Lee et al 2014, for example, propose a BEM-FEM FSI methodology for designing flexible marine

propellers. At higher Reynolds numbers, the flow in the attached fully turbulent boundary layer can be neglected and recovered through a simple correction independent from the potential flow results. The flow on the surface of the propeller is typically in the transitional flow regime for sectional Reynolds number at  $r/R = 0.7$  less than  $1 \cdot 10^6$  (Kuiper 1981). At this Reynolds number, the viscous effects need to be modeled accurately using high fidelity methods like RANSE solvers. At higher loading conditions, the shape of 3D printed propeller can change due to twisting and it can modify total thrust and torque of the propeller.

This presented study deals with low Reynolds number hydrodynamics of 3D printed marine propellers. We show how the propeller open water characteristics (torque and thrust) and distributed hydrodynamic parameters (pressure and shear) can be dramatically influenced by the combined effect of laminar-turbulent transition and blade flexibility under load. We present a simple methodology to calculate the twist in the propeller and then we analyze the change in flow pattern and forces for the twisted propeller.

## 2 Test Case: B-series Propeller

This study builds on the experimental work of Husser and Onas (2018) who built a B-series propeller by fused deposited material 3D printing and then tested the plastic propeller in open water.

### 2.1 Experimental Study

The cited experiments considered low Reynolds numbers in the range  $O(10^5)$ . This was justified by the low strength of the propeller material used (ABS plastic). The authors used Hama strips to stimulate turbulence in this naturally transitional flow regime. For the purpose of this study, we focus only on the propeller tests performed without turbulence stimulators at Reynolds number  $5 \cdot 10^5$ . Geometric characteristics of the B-series propeller are given in Table 1.

The propeller was tested at different speed of revolutions to study its influence on open-water performance. Here, we consider the case  $N = 1100$  rpm, which corresponds to Reynolds number  $5 \cdot 10^5$ .

---

\* Leave blank the last 2.0 cm on the first page to place some additional informational about this paper in a footnote on the first page if necessary.

**Table 1 Geometry of the Wageningen B- series propeller considered in this study**

Parameter	Value
D, D <sub>Hub</sub>	8 in, 1.6 in
Z	4
EAR	0.525
P/D	0.8
N	1100 rpm

## 2.2 Computational Model Setup

The performance of the propeller is calculated using high-fidelity RANSE solver. The fluid is considered incompressible and flow is assumed to be incompressible. The Reynolds-averaged Navier Stokes equation for incompressible Newtonian fluid is given below

$$\frac{\partial u_j}{\partial x_j} = 0 \quad (1)$$

$$\rho \left( \frac{\partial u_i}{\partial t} + u_j \frac{\partial u_i}{\partial x_j} \right) = - \frac{\partial P}{\partial x_i} + \mu \frac{\partial^2 u_j}{\partial x_j \partial x_j} - \frac{\partial \overline{u'_i u'_j}}{\partial x_j} + u'_i \quad (2)$$

where  $\rho$  is the fluid density,  $\mu$  is the dynamic viscosity and  $\overline{u'_i u'_j}$  is the Reynolds stress term. Using Boussinesq eddy viscosity assumption we can relate Reynolds stress to mean strain rate  $S_{ij}$  by the eddy viscosity  $\mu_t$  as follow

$$\overline{u'_i u'_j} = \frac{2}{3} k \delta_{ij} - 2\mu_t S_{ij}; S_{ij} = \frac{1}{2} \left( \frac{\partial u_i}{\partial x_j} + \frac{\partial u_j}{\partial x_i} \right) \quad (3)$$

where  $k$  is the turbulent kinetic energy and  $\delta_{ij}$  is the Kronecker symbol.

Different eddy viscosity model exists which solves additional transport equations to calculate turbulent eddy viscosity (Jones et al 1972, Menter 1994). The propeller in this study operates at Reynolds number  $5 \cdot 10^5$  which lies in transitional flow regime. So, the turbulent eddy viscosity is calculated using the  $\gamma$ - $Re_\theta$  transition model (Menter et al 2006) in this study. The  $\gamma$ - $Re_\theta$  transition model has been recently validated together with other turbulence models for the prediction of laminar-turbulent transitional flow on a hydrofoil (Xu et al 2018).

For open-water performance calculation, the propeller is modeled with a front hubcap and downstream shaft following the open-water configuration. The propeller is modeled as a single blade and periodic interface boundary condition is used to simulate the effect of four blades. This approach is computationally cheaper as compared to modeling all four blades and give the same results as of the whole propeller. The computational domain extends 4D upstream from the propeller plane and 12D downstream from the propeller plane, where D is the diameter of the propeller. The steady-state moving reference frame (MRF) is used. This approach simulates the rotational effect of the propeller by adding rotational body force terms to the Navier-Stokes equation.

The computational domain is discretized using polyhedral cells. There are sufficient prism layers in the boundary

layer such that the wall  $y^+ \approx 1$  on the surface of the propeller. The wall  $y^+ \approx 1$  ensures that no wall functions are used and the transition model can predict the flow transition accurately. The propeller has small curvature radii at the leading and trailing edge. Hence very fine mesh is used in these regions. Volumetric control is used in a region surrounding the propeller to capture the wake correctly. Figure 1 shows the particulars of the mesh on the surface of the propeller and prism layer mesh.

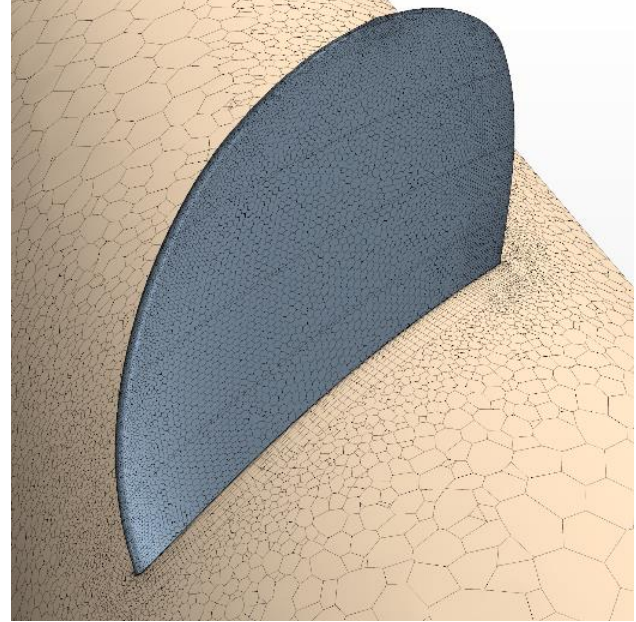


**Figure 1 Mesh particulars from 0.6R to the blade tip**

At the inlet, the velocity inlet boundary condition is used. The velocity of flow is calculated based on the given value of the advance ratio and the rotational speed of the propeller is kept constant at  $N = 1100$  rpm, in analogy with the experimental tests. At the outlet, the pressure outlet boundary condition is used. The propeller and shaft are modeled as wall and no-slip boundary condition is used. The periodic interface boundary condition is used for two surfaces. This boundary condition ensures that there is a conformal mesh mapping between two boundaries and the variables are transferred from one boundary to another.

## 3 Open-water Performance Test

In this section, the experimental open-water performance of the propeller calculated at Reynolds number  $5 \cdot 10^5$  is compared with CFD RANSE solver prediction with the transition model and fully turbulent model. The results are also compared with open-water performance measured at higher Reynolds number  $2 \cdot 10^6$  (Oosterveld et al 1975). Figure 2 shows the comparison of thrust and torque coefficients for experimental results at low Reynolds number performed by Husser & Onas (2018) who found significant differences in their measurement of thrust and torque at low Reynolds number compared to the value obtained from the Wageningen regression curves. This difference can be attributed to different reasons, namely:

- Difference in Reynolds number ( $5 \cdot 10^5$  to  $2 \cdot 10^6$ )

\* Leave blank the last 2.0 cm on the first page to place some additional informational about this paper in a footnote on the first page if necessary.

- Elastic deformation of blades under hydrodynamic loading
- Geometrical differences between the nominal (CAD model) and the physical (3D printed) model

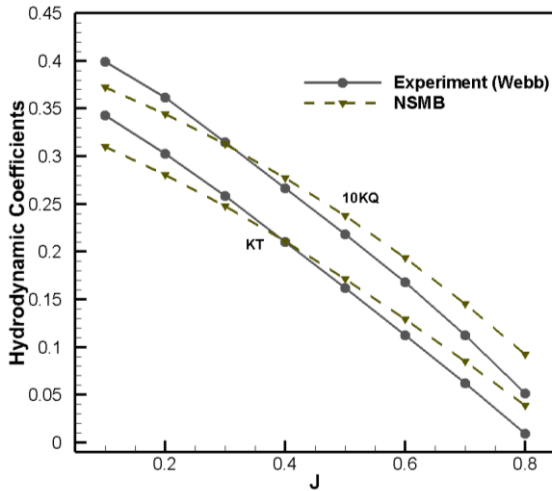


**Figure 2** Open-water performance comparison of the B-series propeller at  $Re=2 \cdot 10^6$  (NSMB) with the experimental results on the 3D printed propeller at low Reynolds number (Webb)

To investigate how big of an effect the partial laminar flow has on the tested low Re propeller, as opposed to the Wageningen results that were obtained in fully turbulent flow, CFD simulations have been run on the rigid propeller calculated using a fully turbulent Reynolds Stress model,  $k-\omega$ -SST, as well as the transitional  $\gamma$ - $Re_{\theta}$  model.

The thrust and torque of the propeller is calculated by integrating the pressure and shear forces over the surface of the blade. The flow in the boundary layer is different between fully turbulent and transition model and hence the forces are different for two models. The torque of the propeller depends upon the skin friction resistance. The skin friction resistance is higher for fully turbulent flow than the laminar flow at same Reynolds number. Therefore, the torque coefficient calculated by fully turbulent model is higher than the transition model and can be seen in Figure 3. Figure 3 also shows the thrust coefficient calculated by fully turbulent model and transition model. The decrease in skin friction leads to small improvement in thrust predicted by the transition model compared to the fully turbulent model.

At lower Reynolds number the flow on the surface of the propeller is in transitional flow regime and the flow direction depends upon the magnitude of the centrifugal and tangential shear force. For transitional flow, the centrifugal force is dominant than the tangential shear force and streamlines are directed in radially outward direction (shown in Figure 4). The limiting streamlines in Figure 4 show the existence of a strong radial flow component on the face of the blade surfaces, caused by the prevalence of centrifugal forces in the low energy near wall region of the laminar boundary layer at advance ratio  $J = 0.5$ . The similar

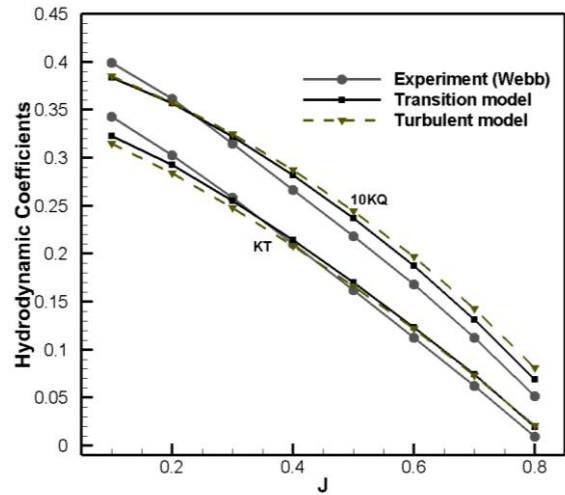


**Figure 3** Numerical results on the rigid B-series propeller with  $k-\omega$ -SST turbulence model and  $\gamma$ - $Re_{\theta}$  transition model and experimental results at low Reynolds number (Webb).

flow pattern is seen at lower advance ratios also and is further discussed in section 5.3.

The radial flow component changes the effective hydrodynamic blade section by moving the trailing edge towards the tip with respect to the leading edge. This leads to a reduction in pitch. This can partly explain the discrepancy noted in experimental study for hydrodynamic forces. For fully turbulent flow, the flow is in tangential direction and the flow starts and ends at same radial location. The effective hydrodynamic pitch will be same as geometrical pitch in case of turbulent flows. Our results for CFD simulations have confirmed the change in hydrodynamic pitch due to modification in streamline direction in transitional flow region.

If we compare the thrust and torque coefficient between the transition model and experimental results at low Reynolds number, we see some similarity in the trend compared to Wageningen regression curves. The thrust and torque coefficients predicted at low Reynolds number by the transition model is higher for low advance ratios ( $J < 0.4$ ) and is lower for high advance ratios ( $J > 0.4$ ) in comparison to experimental results. However, there is still some difference in hydrodynamic forces predicted by the transition model and the experimental results. There might be some geometric differences between the model propeller and actual B-series propeller attributed to errors in the 3D printing process or material deformation while heating the model to remove the wax.

In addition to difference in flow pattern, Husser & Onas (2018) raised the point of deformation due to the twisting of plastic blades at lower advance ratios (high loading) that might have caused an increase in pitch. The thrust and torque coefficients are higher at low advance ratios due to increase in pitch. We further investigated the change in forces due to twisting using a simple approach by applying

the first principle of torsional deflection to rotating propeller. This is presented in the next section.

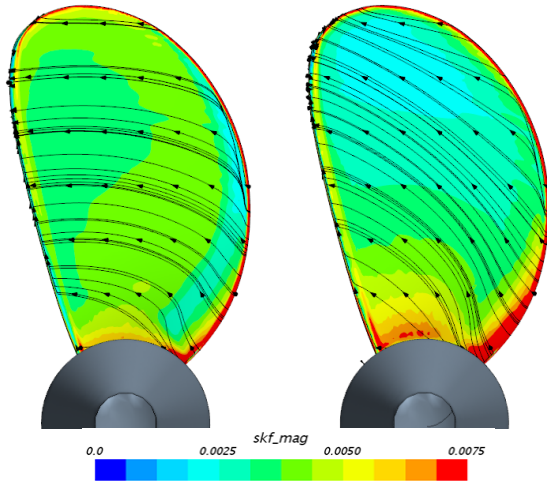


**Figure 4** Local skin friction coefficient and streamlines predicted on the face of the B-series propeller with the fully turbulent  $k-\omega$ -SST (left) and  $\gamma$ - $Re_{\theta}$  trans. model (right)

The mesh is refined in the wake of the propeller using volumetric control option available in StarCCM+. The fine mesh in the wake of the propeller captures the tip vortex as seen in Figure 5. The effect of tip vortex on the flow field around the propeller and hence the forces acting on the propeller is accurately modeled by the CFD solver. The details of mesh in the boundary layer around the propeller blade section at different radial locations are given in Appendix

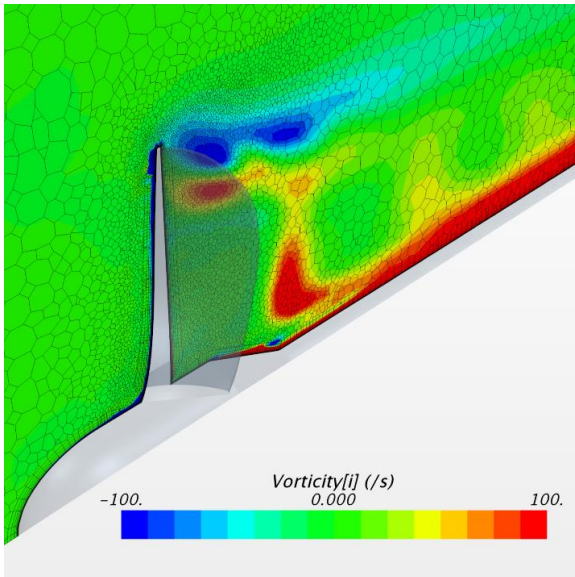


**Figure 5** Tip vortex in the wake of the propeller

#### 4 Twist Calculation

As discussed in Section 3, an increase in propeller pitch due to twisting will result in the higher prediction of thrust and torque coefficients. Husser (2018) formulated an analytical method to quantify the effect of blade twist on open-water performance at model scale. The twist in the propeller can be calculated by applying the first principle of torsional deflection of a slender rod to a rotating

propeller blade. Clearly this is a lower fidelity approach compared to fully coupled fluid structure interaction solvers, where a fully 3D finite element model of the propeller is tightly coupled (at time step level) with the unsteady viscous hydrodynamic solver. These models (Young et al., 2016) are crucial to study flexible propellers intentionally designed to take a controlled twist and deflection under load. The goal of this study is rather to assess the possibility that a blade built to be rigid could have undergone a twist that could have caused the increase in hydrodynamic force measurements. The twist angle along the radius of the propeller can be calculated using the formula given below

$$\delta_r(r, J) = \int_r^{r_{hub}} \frac{N(r, J)}{J(r)G} dr \quad (4)$$

where  $N(r, J)$  is the twisting moment on the blade section at radius  $r$  at the particular advance ratio,  $J(r)$  is the polar moment of inertia of the blade section at radius  $r$ , and  $G$  is the shear modulus of the material. The polar moment of inertia  $J(r)$  can be calculated from the geometry of the

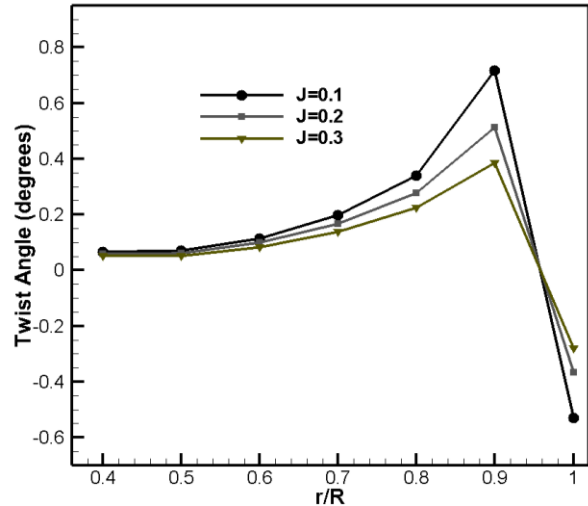


**Figure 6** Radial variation of twist from hub to tip for three different advance ratios  $J = 0.1, 0.2,$  and  $0.3$

propeller at radial location  $r$ . The shear modulus  $G$  depends on the material and is constant from hub to tip. The shear modulus is taken to be 50% of the tensile strength. The twisting moment  $N(r, J)$  depend upon the advance ratio (loading). The twisting moment can be easily calculated from CFD simulation results by integrating the pressure and shear forces and calculating the moment due to these forces about the directrix of the propeller. The material used in the experimental study for 3D printing was VisJet M3 Proplast. The material properties are given in Table 2.

**Table 2** 3D- printed material properties

Parameter	Value
Density ( $g/cm^3$ )	1.02
Tensile Strength (MPa)	42.4
Tensile Modulus (MPa)	1463
Flexural Strength (MPa)	49

## 5 RESULTS AND DISCUSSION

In this section, results are presented for the twist in the propeller at low advance ratios. Also, the results are presented for the difference in global hydrodynamic forces, pressure coefficient and skin friction coefficient for original (untwisted) and twisted propeller at advance ratio  $J = 0.1$ .

### 5.1 Twist of the propeller

The twist of the propeller is calculated using the formula given in section 4 at three advance ratios  $J = 0.1, 0.2$  and  $0.3$  which correspond to higher loading conditions. The variation of twist in the propeller from hub to tip is given in Figure 6. The twist in the blade is very small at lower radii due to lower forces acting in this region. The main contribution of the thrust comes from the region at higher radii. The polar moment of inertia decreases from hub to tip due to reduction chord length and the thickness of the lade section. From Figure 5, we see that the direction of the twist is opposite at the tip of the propeller. Also, the twisting increases with increase in loading (decrease in advance ratio).

### 5.2 Effect on Hydrodynamic Forces

The pitch distribution along the radius of the propeller changes from hub to tip due to twisting as seen in the previous section. The propeller was redesigned with the modified pitch distribution and its performance was again calculated using CFD simulations at advance ratio  $J = 0.1$ .

The total thrust of the original and twisted propeller is given in Table 3. The pressure component of the thrust increases by around 1%. The twist of the propeller causes an increase in pitch of the propeller, especially near the tip. The thrust of the propeller increases due to increase in the pitch. This confirms one of the reasons for higher measurement of thrust force in the experiment by Husser (2018).

**Table 3 Total thrust of the original and twisted propeller at advance ratio  $J = 0.1$**

	Thrust (N)		
	Pressure	Shear	Total
<b>Original</b>	192.86	-0.782	192.1
<b>Twisted</b>	194.39	-0.777	193.6

The total torque of the original and twisted propeller is given in Table 4. The total torque of the twisted propeller is around 3% higher than the original propeller.

**Table 4 Total torque of the original and twisted propeller at advance ratio  $J = 0.1$**

	Torque (N-m)		
	Pressure	Shear	Total
<b>Original</b>	4.417	0.210	4.627
<b>Twisted</b>	4.547	0.204	4.751

### 5.3 Local Flow Characteristics

The pressure distribution on the suction and pressure side of the propeller is given in Figure 9 for the original and twisted propeller at advance ratio  $J = 0.1$ . The pressure coefficient is non dimensionalized using an effective velocity  $V_e = (V_A^2 + (2\pi nr)^2)^{0.5}$  at each radial location. The pressure coefficient on the pressure side is the same for the original and twisted propeller. We see some difference in pressure coefficient contour on the suction side of the original and twisted propeller in the region near the leading edge at lower radii. The variation of pressure coefficient along the chord is plotted at two radial locations  $r/R = 0.8$  and  $0.9$  in Figures 7 and 8. The difference in pressure coefficient can be seen at radial location  $r/R = 0.9$  near the trailing edge.

The distribution of the skin friction coefficient on the face and back of the original and twisted propeller is shown in Figure 12. The direction of the streamlines gives an indication of whether the flow is in the laminar-turbulent region or fully-turbulent flow as discussed in section 3. The skin friction coefficient is non-dimensionalized using an effective velocity  $V_e$  calculated in the same way as the pressure coefficient. The hydrodynamic analysis results in a range of values that corresponds to laminar-turbulent transition for flat plate at Reynolds number  $5 \cdot 10^5$  (Schlichting et al 2016). The streamlines are oriented in the radial direction up to  $r/R = 0.8$  on both suction and pressure side of the propeller at advance ratio  $J = 0.1$ . The flow is directed in the tangential direction at higher radii, which indicates that the flow is fully turbulent at higher radii. The critical radius of at this advance ration is predicted at  $r/R=0.8$ .

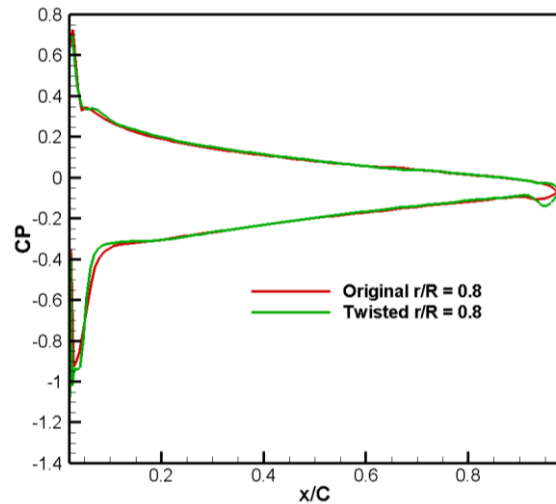


**Figure 7 Pressure coefficient along the chord for two hydrofoil section at radial location  $r/R = 0.8$**

The skin friction coefficient and constrained streamline pattern on the back of the propeller is almost the same for the original and twisted propeller. We see some difference on the face of the original and twisted propellers, especially at higher radii. The angle of attack of flow increases with

an increase in effective pitch due to twisting. The flow separation at the leading edge of the hydrofoil changes with the change in angle of attack. We can see the difference in skin friction coefficient near the leading edge on the pressure side for the original and twisted propeller.

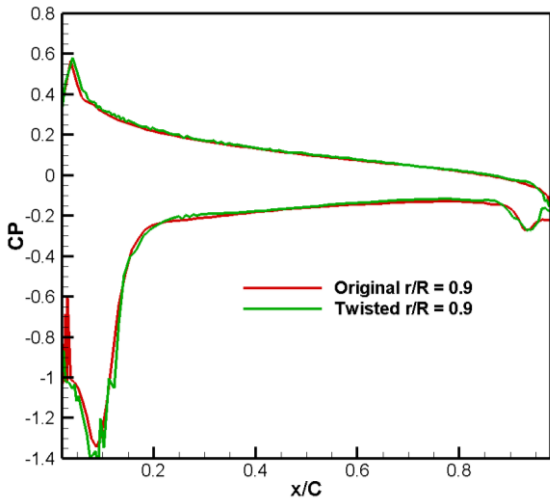


Figure 8 Pressure coefficient along the chord for two hydrofoil section at radial location  $r/R = 0.9$

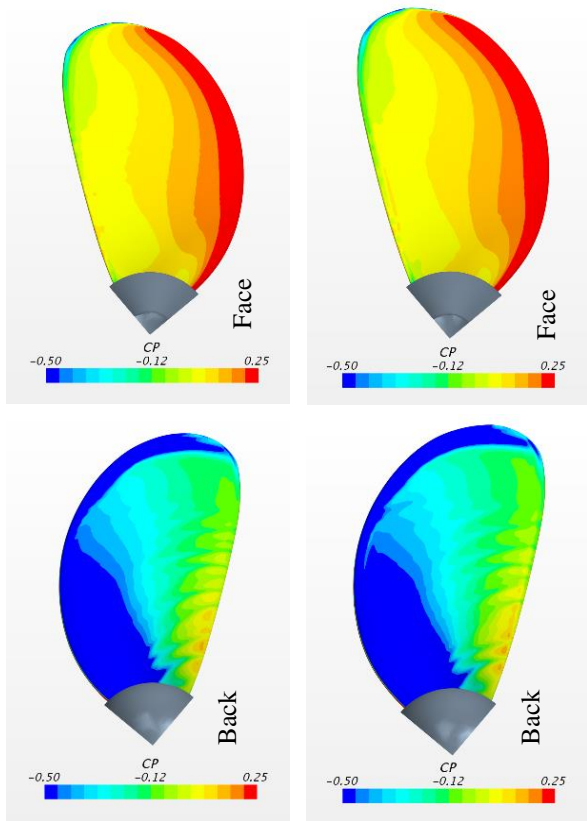


Figure 9 Pressure coefficient contour on the surface of the original and twisted propeller at advance ratio  $J = 0.1$  left: original, right: twisted

The skin friction coefficient is plotted along the chord for two radial locations  $r/R = 0.8$  and  $0.9$  in Figures 10 and 11. It can be seen that the skin friction coefficient is different between original and twisted propeller near the trailing edge on the face for the original and twisted propeller. This is due to a shift of the laminar-turbulent natural transition point predicted on the twisted propeller. The flow separation occurs early at higher radii near the tip of the propeller for original propeller compared to the twisted propeller as can be seen from Figures 10 and 11.

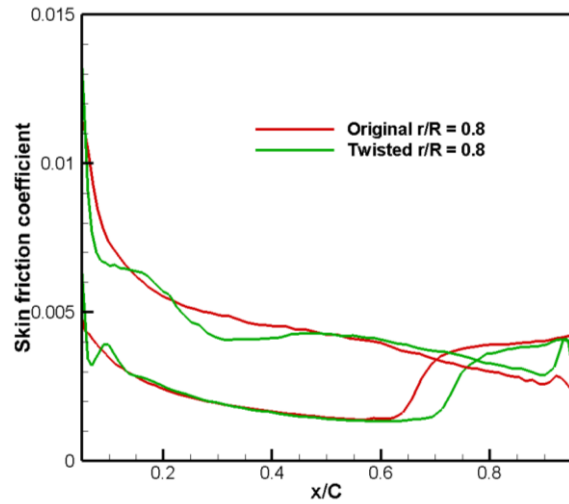


Figure 10 Skin friction coefficient along the chord for the same section at  $r/R = 0.8$  on the rigid (original) and twisted propeller

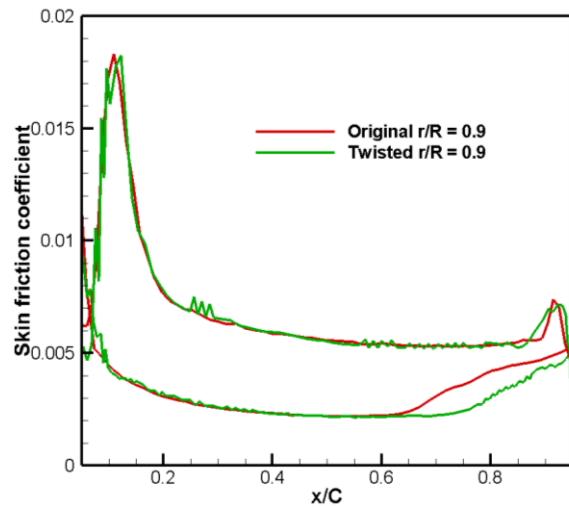
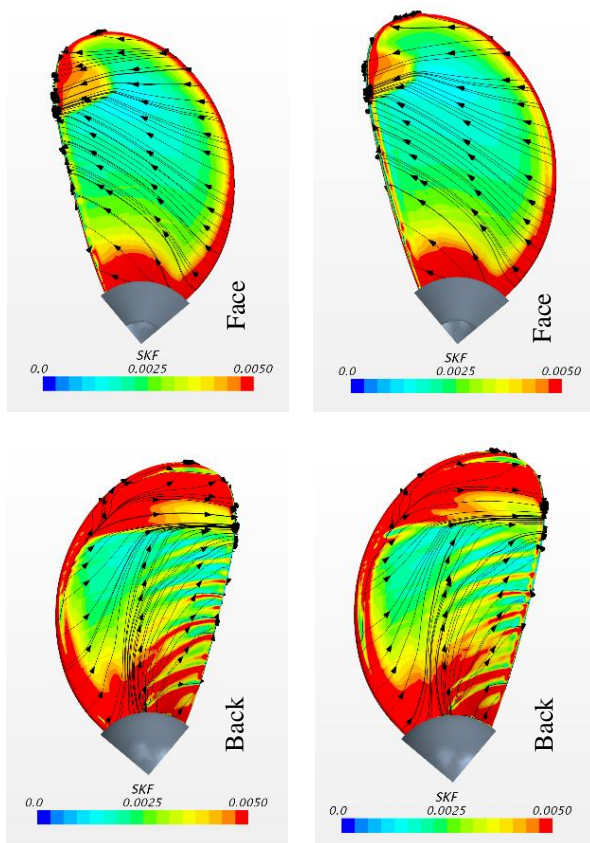


Figure 11 Skin friction coefficient along the chord for the same section at  $r/R = 0.9$  on the rigid (original) and twisted propeller



**Figure 12** Skin friction coefficient contour on the surface of the original and twisted propeller at advance ratio  $J = 0.1$  left: original, right: twisted

## 6 Conclusion

The performance of 3D printed marine propeller is investigated in this study at low Reynolds number. The performance of propeller at low Reynolds number is different from when it is operating in fully turbulent flow.

At low Reynolds number, the hydrodynamic forces acting on the propeller gets modified. This is due to the change in the effective pitch of the propeller. The boundary layer on the surface of the propeller is different at low Reynolds number than fully turbulent flow. The frictional drag is a function of Reynolds number influences the development of the boundary layer on the surface of the propeller. The change in effective pitch and boundary layer alters the hydrodynamic behavior of propeller at low Reynolds number. The hydrodynamic coefficients calculated using CFD simulations at low Reynolds number are lower than the hydrodynamic coefficients at higher Reynolds number at high advance ratios (low loading). This trend is opposite at low advance ratios (higher loading), where the hydrodynamic coefficients are higher for low Reynolds number flow. These findings are consistent with the experimental measurement for the open-water performance of the propeller at low Reynolds number.

Since the 3D printed plastic is not as strong as the metal or composite material the propeller can get deformed at higher loading condition due to twisting. The twist angle of

the propeller was calculated using a simple analytical expression based on the principle of torsional deflection of a uniform beam. This simple approach can give an approximate estimate of the change in pitch of the propeller due to twisting. The twisted propeller with the modified pitch distribution was simulated at advance ratio  $J = 0.1$ . The maximum twist angle was calculated to be around 0.8 deg. This change in pitch angle is able to make a difference on the propeller performance because it directly changes the angle of attack at the most representative blade sections. The thrust coefficient and torque coefficient of the twisted propeller is around 1% and 3% higher than the original propeller at Reynolds number  $5 \cdot 10^5$ . As the shape of the propeller changes, the forces and twisting moment also changes which in turn modifies the propeller shape. Hence an iterative method should be developed which will automatically change the shape of the propeller till equilibrium is attained.

The methodology presented in this study does not couple the fluid and solid solver. The preliminary findings of this study indicate that 3D printed marine propeller undergoes deformation due to twisting and should be modeled using fluid-structure interaction (FSI) model. CFD-FEA FSI model can accurately model the twisting of the propeller and will remove the user intervention to modify the geometry and run the simulation again.

## ACKNOWLEDGMENTS

The authors would like to thank Mr. Nickolas Husser for his help in generating the 3D model of the twisted propeller, in a consistent way to the original propeller he tested in his experiments.

The support of the Office of Naval Research, grant N00014-16-1-2589, P.M. Reginald Beach and grant N00014-17-1-2347, P.M. Woei-Min Lin, is gratefully acknowledged.

## REFERENCES

- Husser, N. A., & Onas, A. S. (2018). An Investigation of Turbulence Stimulation on 3D Printed Model Propellers. Proceedings SNAME Maritime Convention. The Society of Naval Architects and Marine Engineers.
- Jones, W. P., & Launder, B. E. (1972). The prediction of laminarization with a two-equation model of turbulence. *International journal of heat and mass transfer*, 15(2), 301-314.
- Kuiper, G. (1981). Cavitation inception on ship propeller models. PhD Thesis, Delft University (NL).
- Lee, H., Song, M. C., Suh, J. C., & Chang, B. J. (2014). Hydro-elastic analysis of marine propellers based on a BEM-FEM coupled FSI algorithm. *International Journal of Naval Architecture and Ocean Engineering*, 6(3), 562-577.
- Menter, F. R. (1994). Two-equation eddy-viscosity turbulence models for engineering applications. *AIAA journal*, 32(8), 1598-1605.

- Menter, F. R., Langtry, R. B., Likki, S. R., Suzen, Y. B., Huang, P. G., & Völker, S. (2006). A correlation-based transition model using local variables—part I: model formulation. *Journal of turbomachinery*, 128(3), 413-422.
- Oosterveld, M. W. C., & van Oossanen, P. (1975). Further computer-analyzed data of the Wageningen B-screw series. *International Shipbuilding Progress*, 22(251), 251-262.
- Portner, S. M. (2014). Design of a low Reynolds number propulsion system for an autonomous underwater vehicle (Doctoral dissertation, Virginia Tech).
- Schlichting, H., & Gersten, K. (2016). *Boundary-layer theory*. Springer.
- Stanway, M. J., & Stefanov-Wagner, T. (2006). Small-diameter ducted contrarotating propulsors for marine robots. In *OCEANS 2006* (pp. 1-6). IEEE.
- Xu, L., Baglietto, E., & Brizzolara, S. (2018). Extending the applicability of RANS turbulence closures to the simulation of transitional flow around hydrofoils at low Reynolds number. *Ocean Engineering*, 164, 1-12.
- Young, Y.L., Motley M., Barber R., Chae E.J., Garg N. (2016). Adaptive Composite Marine Propulsors and Turbines: Progress and Challenges. *Applied Mechanics Reviews*. 68. DOI:10.1115/1.4034659.

## Appendix

The mesh around the blade section at different radial location is shown in Figure 13

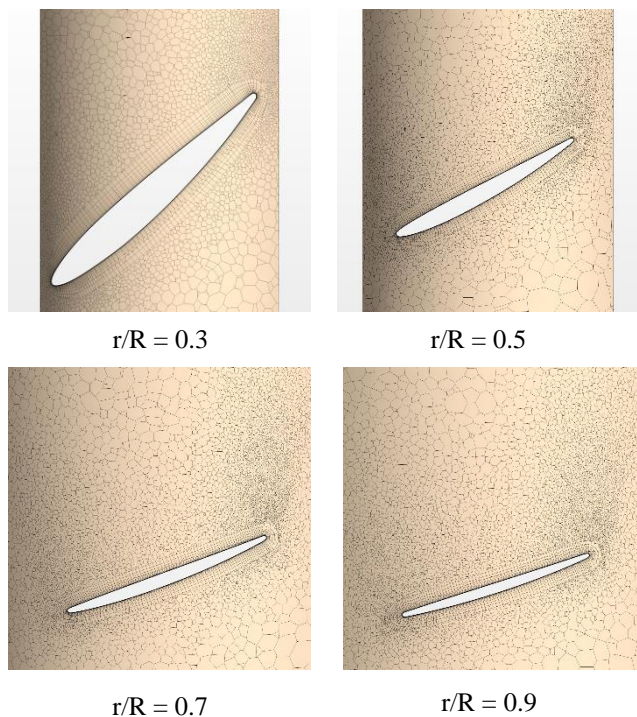


**Figure 13** Particulars of mesh in the boundary layer for the propeller at different radial locations